Monthly Notices of the ROYAL ASTRONOMICAL SOCIETY

MNRAS **465,** 4468–4481 (2017) doi:10.1093/mnras/stw2890
Advance Access publication 2016 November 10

The nova-like nebular optical spectrum of V404 Cygni at the beginning of the 2015 outburst decay

Farid Rahoui,[1,2]★ J. A. Tomsick,[3] P. Gandhi,[4] P. Casella,[5] F. Fürst,[6] L. Natalucci,[7] A. Rossi,[8] A. W. Shaw,[4] V. Testa[5] and D. J. Walton[6]

[1]*European Southern Observatory, K. Schwarzschild-Str 2, D-85748 Garching bei München, Germany*
[2]*Department of Astronomy, Harvard University, 60 Garden street, Cambridge, MA 02138, USA*
[3]*Space Sciences Laboratory, 7 Gauss Way, University of California, Berkeley, CA 94720-7450, USA*
[4]*Department of Physics and Astronomy, University of Southampton, Highfield, Southampton SO17 1BJ, UK*
[5]*INAF-OA Roma, Via Frascati 33, I-00078 Monteporzio Catone, Italy*
[6]*California Institute of Technology, 1200 East California Boulevard, Pasadena, CA 91125, USA*
[7]*Istituto di Astrofisica e Planetologia Spaziali, INAF, Via Fosso del Cavaliere 100, I-00133 Roma, Italy*
[8]*INAF-IASF Bologna, Area della Ricerca CNR, via Gobetti 101, I-40129 Bologna, Italy*

Accepted 2016 November 7. Received 2016 November 4; in original form 2016 June 17

ABSTRACT

We report on FORS2 optical spectroscopy of the black hole X-ray binary V404 Cygni, performed at the very beginning of its 2015 outburst decay, complemented by quasi-simultaneous *Swift* X-ray and ultraviolet as well as Rapid Eye Mountain near-infrared observations. Its peculiar spectrum is dominated by a wealth of emission signatures of H I, He I, and higher ionization species, in particular Fe II. The spectral features are divided between broad redshifted and narrow stationary varieties, the latter being emitted in the outer regions. Continuum and line variability at short time-scale is high, and we find Baldwin effect-like anticorrelations between the full widths at half-maximum and equivalent widths of the broad lines with their local continua. The Balmer decrement Hα/Hβ is also abnormally large at 4.61 ± 0.62. We argue that these properties hint at the broad lines being optically thick and arising within a circumbinary component in which shocks between faster optically thick and slower optically thin regions may occur. We associate it to a nova-like nebula formed by the cooling remnant of strong accretion disc winds that turned off when the mass-accretion rate dropped following the last major flare. The Fe II lines likely arise from the overlap region between this nebula and the companion star winds, whereas we favour the shocks within the nebula as responsible for the optical continuum via self-absorbed optically thin bremsstrahlung. The presence of a near-infrared excess also points towards the contribution of a strongly variable compact jet or a dusty component.

Key words: accretion, accretion discs – binaries: close – stars: individual: V404 Cygni – ISM: jets and outflows – X-rays: binaries.

1 INTRODUCTION

On 2015 June 15, the Burst Alert Telescope instrument (Barthelmy et al. 2005) mounted on the *Swift* satellite (Gehrels et al. 2004) detected the Galactic black hole (BH) X-ray binary (XRB) V404 Cygni after 26 yr of quiescence (Barthelmy et al. 2015). The rarity of such an event triggered a collaborative multiwavelength observational campaign of unprecedented scale and despite its brevity, the extreme behaviour exhibited by the source has puzzled the community. Indeed, unlike most of other microquasars whose outbursts can be well described by hysteresis-like (or q-shape) hardness intensity diagrams tracing spectral transitions between corona-dominated hard states and disc-dominated soft states (Fender, Belloni & Gallo 2004), V404 Cygni underwent several hard X-ray flares with up to 10-fold flux variations within a few hours. Whether it transitioned between different spectral states is not clear, several authors having claimed that it was always caught in the hard state (see e.g. Natalucci et al. 2015; Rodriguez et al. 2015; Jenke et al. 2016), while Radhika et al. (2016) argue that it went through several transitions within each flare. The origin of these flaring events has not been clarified yet, but several studies point towards hard X-ray spectra stemming from Compton scattering of relatively hot photons, maybe from the jets (Natalucci

★ E-mail: farid@rahoui.eu

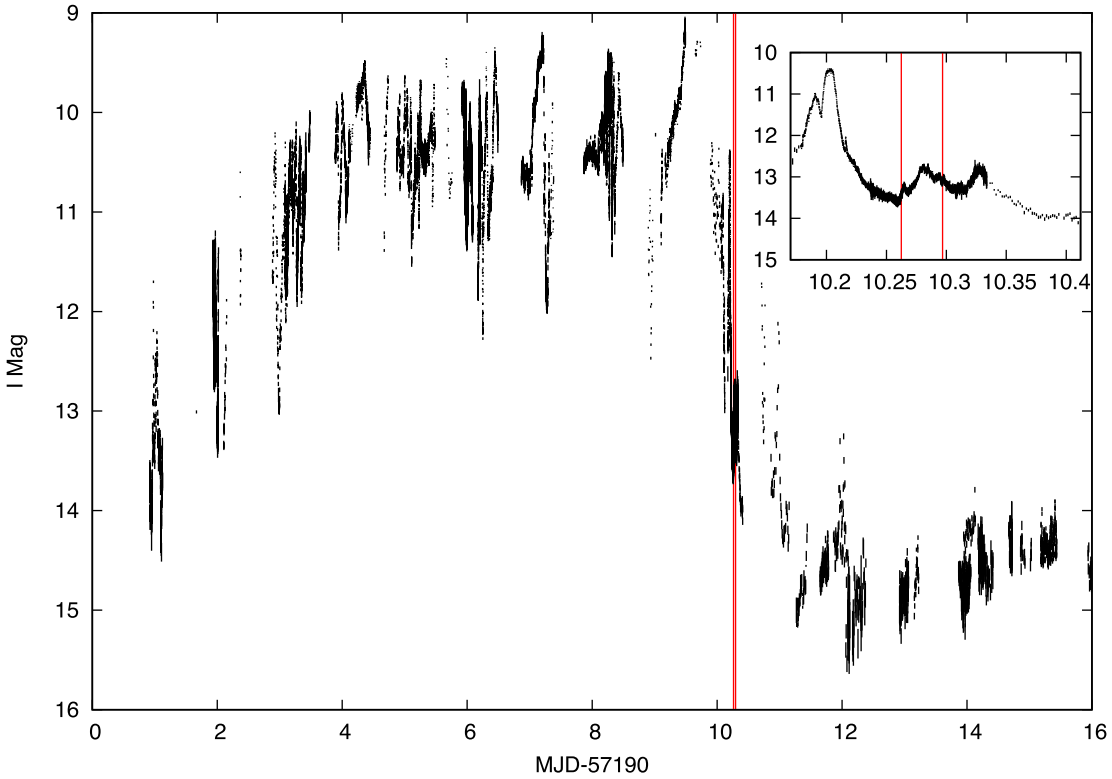

Figure 1. V404 outburst as seen through *I*-band photometry. The red vertical bars mark the time range of our FORS2 observations, and the inset displays a zoom-in centred on the FORS2 epoch.

et al. 2015; Jenke et al. 2016), while *Chandra* and GTC/OSIRIS spectroscopic observations hint at the likely presence of a strong quasi-spherical accretion disc wind (ADW) detected via narrow soft X-ray emission lines (King et al. 2015) as well as optical P-Cygni profiles (Muñoz-Darias et al. 2016). Finally, this extreme variability pattern was not restricted to the X-ray domain and was observed in all bands, including fast radio flares from transient jets (Mooley, Clarke & Fender 2015; Tetarenko et al. 2015b), as well as sub-second optical photometric flickering associated with optically thin synchrotron from compact jets (Gandhi et al. 2016).

As one of the brightest microquasars at optical wavebands, both in outburst and quiescence, V404 Cygni has been extensively studied in this spectral domain. During the 1989 outburst, several authors reported very rich optical spectra dominated by strong emission signatures from H I and He I as well as higher ionization elements (see e.g. Casares et al. 1991; Gotthelf et al. 1992). The continuum and lines were found to be strongly variable, and various morphologies were observed, including single- to triple-peaked features as well as transient P-Cygni profiles; some of these characteristics were again observed during the 2015 outburst (see e.g. Muñoz-Darias et al. 2016). The system's properties are also relatively well constrained, and V404 Cygni consists of a K0-3IV star orbiting a BH with a 6.08 ± 0.06 $M_{\odot}$ mass function in 6.4714 ± 0.0001 d, the secondary-to-primary mass ratio being $q = 0.060^{+0.004}_{-0.005}$ (Casares, Charles & Naylor 1992; Casares & Charles 1994; Khargharia, Froning & Robinson 2010). Its distance was also assessed via accurate radio parallax measurements at 2.39 ± 0.14 kpc (Miller-Jones et al. 2009), but the inclination of the system remains relatively unknown, with values ranging from 50° to 70°, which leads to a poorly constrained BH mass in the range 8–15 $M_{\odot}$ (Shahbaz et al. 1994; Khargharia et al. 2010).

In this paper, we report on medium-resolution optical spectroscopy of V404 Cygni – complemented by X-ray, ultraviolet, and near-infrared data – performed right after the last major flare, at the very beginning of its decay to quiescence (see Fig. 1). Section 2 details the data reduction procedure, whereas Section 3 is dedicated to the spectral analysis. We discuss the outcomes and their implications in Section 4 and conclude in Section 5.

2 OBSERVATIONS AND DATA REDUCTION

The data set consists of quasi-simultaneous observations obtained on 2015 June 27, with (1) the FOcal Reducer/Low disperser Spectrograph 2 (Obs. ID 095.D-0459, PI: Rahoui; FORS2; Appenzeller et al. 1998) mounted on the UT1 Cassegrain focus at the European Southern Observatory (ESO) Very Large Telescope (VLT) at Cerro Paranal; (2) the X-Ray Telescope (XRT; Burrows et al. 2005) and Ultra-Violet/Optical Telescope (UVOT; Roming et al. 2005) on board the *Swift* (Gehrels et al. 2004) satellite (Obs. ID 00031403061, Public; Obs. ID 00033861002, PI: Altamirano); (3) the Joint European X-ray Monitor (JEM-X; Lund et al. 2003) and Imager On board *INTEGRAL* Satellite (IBIS; Ubertini et al. 2003) mounted on the *INTERnational Gamma-Ray Astrophysics Laboratory* (*INTEGRAL*; Winkler et al. 2003) satellite (Science Window ID 155700300010, 155700320010, and 155700340010); and (4) the Rapid Eye Mount IR (REMIR; Obs. ID 29023, PI: Casella; Calzoletti et al. 2005) installed on the Rapid Eye Mountain (REM) telescope at Cerro La Silla. For the sake of building a radio to X-ray spectral energy distribution (SED), we also use quasi-simultaneous radio data obtained with the RATAN-600 radio telescope at 2.3, 4.6, 8.2, 11.2, and 21.7 GHz (Trushkin, Nizhelskij & Tsybulev 2015) between MJD 57199.9 and MJD 57200.7, as well as 97.5 and 140.5 GHz flux densities from the NOrthern Extended Millimeter Array (NOEMA)

and integrated between MJD 57199.3 and MJD 57200.1 (Tetarenko et al. 2015a).

2.1 FORS2 observations

On 2015 June 27, we performed FORS2 medium-resolution spectroscopy of V404 Cygni (see Fig. 1) with the 600V (hereafter *V*) and 600I (hereafter *I*) grisms combined with the GC435 and OG590 filters, respectively, for a total 4500–9300 spectral coverage. In both cases, we used the standard resolution (SR) collimator and the slit-width was set to 1 arcsec with a rotation angle always close to the parallactic angle. Atmospheric conditions were medium to good, with a thin sky transparency and a 1.91 airmass. The exposure time of each individual frame was set to 30 s, and a total of 20 and 19 exposures were taken in both *V* and *I*, respectively, which, accounting for overheads, gives a 67 s effective time resolution for variability study. The A0V spectro-photometric standard star LTT 7379 was observed in similar conditions for flux calibration.

We reduced the data using the dedicated pipeline (v. 5.3.5) implemented in the ESO data reduction environment `Reflex` v. 2.6 (Freudling et al. 2013), which follows the standard steps for optical spectroscopy reduction and produces cleaned and background subtracted 2D spectroscopic images. The wavelength calibration was achieved by deriving a dispersion solution using helium, argon, and mercury/cadmium arc observations. We then used the routines `apall`, `standard`, `sensfunc`, and `calibrate` implemented in IRAF v. 2.16[1] to optimally extract the source, sky, and spectro-photometric standard star 1D spectra, compute the sensitivity function, and apply it to V404 Cygni *V* and *I* spectra for flux calibration. The accuracy of the dispersion solution was finally assessed by measuring the centroids of the brightest OH emission lines present in the sky spectra. We found systematic +0.6 to +0.8 Å offsets, likely due to the 5 h time gap between the science and arc observations. A −0.8 Å correction was thus applied to all line centroid measurements listed in this study. When applicable, we also corrected all listed radial velocity shifts for a 13 km s^{-1} barycentric–heliocentric velocity as estimated at the epoch of the observations.

The flux-calibrated spectra were corrected for slit losses, which we estimated assuming the slit transmission factor used by ESO for its exposure time calculators.[2] It consists in an error function *erf* that depends on the slit-width and the image quality at the focal plane of the telescope. We slightly modified it to include potential slit-centring offsets implied by the wavelength-dependent atmospheric differential refraction for a given airmass and rotation angle, as formulated in Filippenko (1982). The wavelength dependence of the image quality along the slit was modelled using the expression given in Martinez et al. (2010), which takes into account the combined effects of the airmass and the outer scale of the turbulences. The reference image quality was directly measured on each individual 2D spectroscopic frame at 5015 and 7065 Å in *V* and *I*, respectively, through Gaussian fitting of the spatial profiles, and we find values in the range 0.6–0.8 arcsec. We stress here that our observations were seeing-limited and the spectral resolution was thus better than the one expected when a source fully fills the slit. Through the fit to the full widths at half-maximum (FWHMs) of the arc lines, we measure the slit-limited resolution between $R \sim 1100$–1500 and $R \sim 1400$–1900 in *V* and *I*, respectively. The seeing-limited resolution being roughly equal to the slit-limited one divided by the image quality, we consequently reached $R \sim 1200$–1900 and $R \sim 2200$–2900 in *V* and *I*, respectively.

Finally, based on the continuum level gap between *V* and *I* in the overlap region, we estimate that the flux calibration is accurate at 3 per cent, although the statistical noise is a lot lower. Moreover, we derive $V = 15.72 \pm 0.03$ and $I = 12.90 \pm 0.03$ through the convolution of the average flux-calibrated spectrum with Johnson and Cousins filters, whereas the average simultaneous AAVSO magnitudes during our observations are $V = 15.67 \pm 0.05$ and $I = 12.95 \pm 0.01$.

2.2 *Swift* observations

We reduced the XRT data with HEASOFT v. 6.17 and the 2016 January 20 calibration data base (CALDB) version. We used XRTPIPELINE v. 0.13.1 to collect events in Windowed Timing (WT) mode to avoid pile-up. For Obs. ID 00031403061, the source and background spectra were extracted with XSELECT v. 2.4c using 40-pixel square boxes in the 0.4–10 keV energy range. We generated the ancillary response file (ARF) with `xrtmkarf` and used the latest version (v. 015) of the response matrices provided by the *Swift* team. We rebinned the spectrum to obtain a minimum of 50 counts per channel, and restricted the effective energy range to 0.4–5 keV as the source is not detected beyond.

In contrast, the XRT data for Obs. ID 00033861002 appeared clearly extended towards the south–west direction without the clear presence of a point source. This is likely due to the formation of the X-ray dust-scattered rings reported in Beardmore et al. (2015) and Vasilopoulos & Petropoulou (2016). For this reason, no spectrum was extracted, and we decided not to use these data for this study.

The UVOT photometry was obtained in two filters, *W*1 for Obs. ID 00031403061 and *U* for Obs. ID 00033861002. We produced an image in each of them with `uvotimsum`. We then used `uvotsource` to extract the source in a 5 arcsec region and the background counts in a 15 arcsec source-free circular aperture, respectively. The derived V404 Cygni flux densities are $(7.89 \pm 0.89) \times 10^{-16}$ and $(1.79 \pm 0.09) \times 10^{-16}$ erg cm^{-2} s^{-1} $Å^{-1}$ in *W*1 and *U*, respectively.

2.3 *INTEGRAL* observations

The data were reduced with the `jemx_science_analysis` and `ibis_science_analysis` routines implemented in the Off-Line Scientific Analysis (OSA) v10.2 suite using the most recent calibration files. Images were first generated in 16 bands between 3.04 and 34.88 keV for the two JEM-X instruments whereas four bands were used for the IBIS Soft Gamma-Ray Imager (ISGRI; Lebrun et al. 2003), covering the range 20–200 keV. A careful analysis of all produced images showed that V404 Cygni was detected in all JEM-X and ISGRI bands during the first two science windows but only with JEM-X below 16 keV during the third one, which is simultaneous to our FORS2 observations. We then extracted JEM-X and ISGRI spectra at V404 Cygni *Chandra* position and generated redistribution matrix files (RMFs) rebinned to the spectral ranges of interest.

2.4 REM observations

The REM data were taken on 2015 June 27 with REMIR in *J*, *H*, and K_s and consist in a sequence of three images per filter, each image being constituted of five frames that were dithered using a prism

[1] IRAF is distributed by the National Optical Astronomy Observatories, which are operated by the Association of Universities for Research in Astronomy, Inc., under cooperative agreement with the National Science Foundation.

[2] https://www.eso.org/observing/etc/doc/formulabook/node18.html

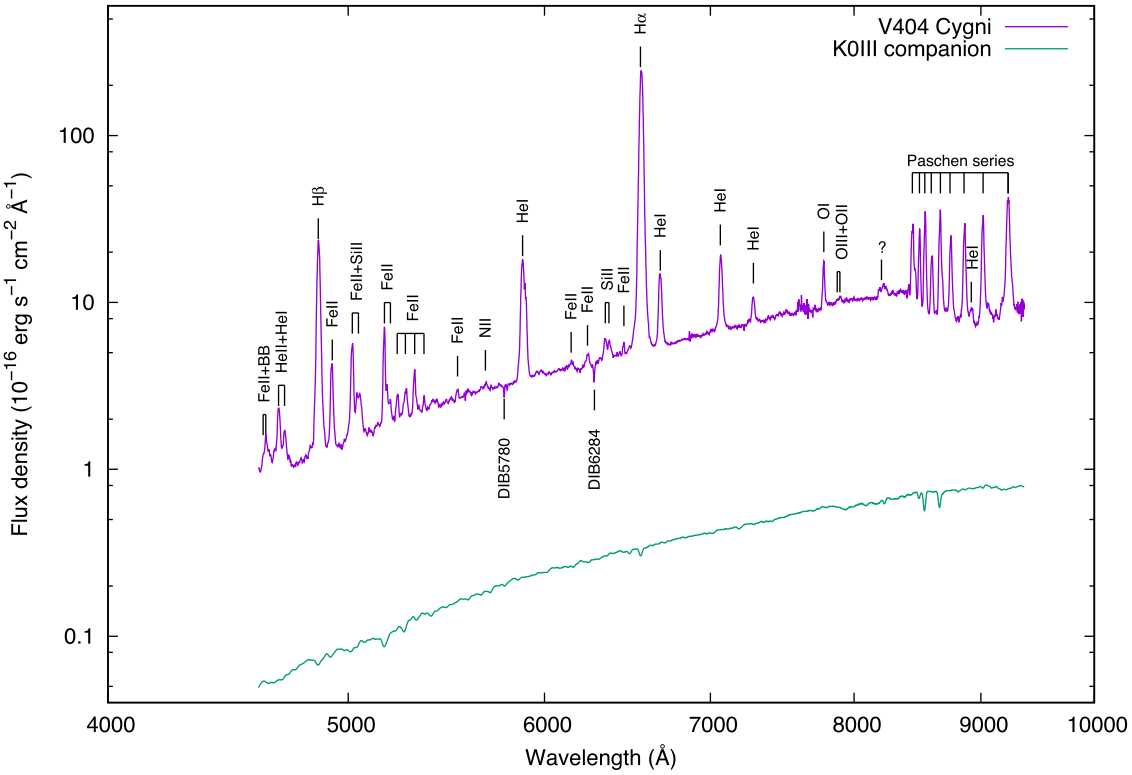

Figure 2. Flux-calibrated time-averaged FORS2 spectrum of V404 Cygni (magenta) compared to that of a K0III giant star suffering from the same ISM extinction and scaled to V404 Cygni companion star's optical magnitudes (green). All the detected emission lines and DIBs are marked.

wedge. The reduction process, done automatically by the robotic Automatic Quick Analysis pipeline (Testa et al. 2004), consisted in first obtaining an empty sky image from a median stack of the five dithered frames and subtracting it from each of them. Following the application of a flat-field image, the images were re-aligned and stacked to obtain a final image with a signal-to-noise ratio (S/N) equivalent to the total exposure time of the five-image sequence. Photometry was then performed using the Point Spread Function (PSF)-fitting software DAOPHOT (Stetson 1987), and the fluxes were calibrated using some secondary standard stars in the field against the Two Micron All Sky Survey (2MASS) catalogue (Skrutskie et al. 2006) . We measure the following magnitudes: 11.40 ± 0.06, 11.35 ± 0.05, and 11.37 ± 0.05 in J, 10.72 ± 0.08, 10.80 ± 0.08, 10.85 ± 0.08 in H, and 10.25 ± 0.09, 10.24 ± 0.07, and 10.33 ± 0.08 in K_s.

3 RESULTS

Fig. 2 displays the 4500–9300 Å slit-loss-corrected average spectrum of V404 Cygni. The expected contribution from its companion star, modelled by a K0III spectrum scaled to the disc contribution-corrected magnitudes derived in Casares et al. (1993) when the source was in quiescence and reddened to the Interstellar Medium (ISM) extinction along the line of sight of the source (see below), is also displayed. The detected lines, the measurements of which are listed in Table 2, are also marked. We give their measured wavelength λ_c and laboratory wavelength λ_l in Å, radial velocity shifts ΔV in km s^{-1} if any, equivalent widths $\mathring{W}$ in Å, FWHMs in km s^{-1}, quadratically corrected from the instrumental FWHMs, as well as their intrinsic fluxes in erg cm^{-2} s^{-1}. Note that their underlying continuum was locally assessed with a first-order polynomial. The latter being the primary source of inaccuracy, each measurement was repeated several times with different continuum placements within the same wavelength range to obtain a set of values that eventually averaged out. The uncertainties listed in Table 2 are therefore the scatter to the mean rather than the statistical errors for any one fit, which are much smaller.

3.1 The optical spectroscopic content

V404 Cygni optical spectrum is very rich, with a wealth of HI (Hα, Hβ, the Paschen series), He I and He II emission lines. We report a weak C III+N III fluorescence complex (also called the Bowen Blend, BB) around 4640 Å that likely originates from the irradiated accretion disc as our observations took place at $\phi \approx 0.05$ (see Table 1), i.e. when the emission from the irradiated hemisphere of the companion star is not visible to the observer. We moreover detect several less common emission features, most of which we associate with Fe II along with some signatures of Si II, O I, O II, O III, and N II, which were not present at the beginning of the outburst (Bernardini et al. 2016). An unidentified complex, which might as well be an instrumental feature as a blend of He I and He II lines, is also present around 8223 Å.

This spectroscopic content is consistent with that reported in some previous studies of the 1989 outburst (Casares et al. 1991; Wagner et al. 1991; Gotthelf et al. 1992). Yet, despite having a similar continuum flux level, Hα and Hβ are 50 and 20 times brighter, respectively, than during 1989 July 1–4 observations presented in Gotthelf et al. (1992). This explains why their equivalent widths are so much larger than those previously reported, with $\mathring{W}_{H\alpha} \approx -1130$ Å and $\mathring{W}_{H\beta} \approx -241$ Å in the FORS2 spectrum compared with about −110 and −12 Å, respectively, in 1989 July 1–4.

Table 1. Summary of V404 Cygni observations and archival data we made use of in this study. The orbital phase ϕ of the BH was estimate using the ephemeris given in Casares & Charles (1994).

Facilities	ID	Instrumental configuration	Start date (MJD)	Exp. Time (s)	ϕ
ESO VLT	095.D-0459	FORS2/GC435+600V, OG590+600I	57200.2661	600, 570	0.05–0.06
INTEGRAL	155700300010	JEM-X-1, JEM-X-2, ISGRI	57200.1179	2620, 2597, 2075	0.03–0.04
”	155700320010	”	57200.1904	2570, 2551, 2046	0.04–0.05
”	155700340010	”	57200.2629	2587, 2584, 2064	0.05–0.06
Swift	00031403061	XRT, UVOT/*W*1	57200.1388	58, 73	0.03
”	00033861002	XRT, UVOT/*U*	57200.3925	1475, 1494	0.07–0.08
ESO REM	29023 (AOT29)	REMIR/*J*, *H*, K_s	57200.2899	50, 50, 50	0.06
AAVSO	–	*V*, *I*	57200.2658	–	0.05–0.06
IRAM	–	NOEMA/97.5 GHz, 140.5 GHz	57199.3000	5400, 9000	0.86–0.97
RATAN-600	–	2.3 GHz, 4.6 GHz, 8.2 GHz, 11.2 GHz, 21.7 GHz	57199.9000	–	0.97–0.09

Hα also has very broad wings of $\pm$2000 km s^{-1}. Complex and variable line profiles were previously reported, including double- and triple-peaked emissions as well as P-Cygni profiles (Muñoz-Darias et al. 2016). In our case, although the 1100–1900 average resolution of the FORS2 spectra prevents a detailed analysis, it is very likely that all the features are single peaked. HI $\lambda\lambda$8865, 9015, and 9229 profiles do show two local maxima, but we do not believe that those are physical.

Based on their radial velocities, the features are separated between stationary and redshifted, pointing towards at least two components responsible for V404 Cygni optical emission. Most of the higher ionization species, in particular Fe II and Si II, as well as Pa (17-3) to Pa (11-3), do not exhibit any velocity shift, although we stress that the uncertainties on the centroid measurements are sometimes quite large, and we cannot rule out that some of them are actually displaced. Pa (10-3) and Pa (9-3) centroids do show +20 to +30 km s^{-1} shifts but they are likely not physical. In contrast, Hβ, He I λ5876, Hα, He I λ6678, He I λ7065, He I λ7281, and O I λ7774 are unambiguously redshifted, with radial displacements ranging between about +70 and +120 km s^{-1}.

Finally, besides features intrinsic to V404 Cygni, we searched for diffuse interstellar bands (DIBs) and we report two centred at 5780 and 6284 Å. Herbig (1975) showed that DIBs were strongly correlated to the ISM extinction along the line of sight of the sources in which they are detected and derived several relationships between their equivalent widths and $E(B-V)$. Here, we nonetheless rely on DIB5780 only as DIB6284 is likely contaminated with some atmospheric absorption troughs. Jenniskens & Desert (1994) obtained $\mathring{W}_{5779} = (0.647 \pm 0.053) \times E(B-V)$. We measure $\mathring{W}_{5779} = 0.798 \pm 0.027$ Å which leads to $E(B-V) = 1.233 \pm 0.116$. For an average total-to-selective extinction ratio $R_V = 3.1$, we thus derive $A_V = 3.82 \pm 0.36$, in line with previous estimates (see e.g. Hynes et al. 2009). We note that this A_V value is consistent with a distance in the range 2.4–2.8 kpc as derived using the 3D extinction map given in Marshall et al. (2006), which is similar to the 2.39 $\pm$ 0.14 kpc distance measured through radio parallax and reported in Miller-Jones et al. (2009).

3.2 The optical spectroscopic variability

During this outburst, V404 Cygni emission has been highly erratic and extreme multiwavelength variations were reported by several authors (Tetarenko et al. 2015b; King et al. 2015; Rodriguez et al. 2015; Kimura et al. 2016; Martí, Luque-Escamilla & García-Hernández 2016; Rana et al. 2016). A strong variability pattern with FORS2 is therefore expected, and the fact that both *V* and *I* observations consist of 20 and 19 sub-exposures of 30 s each, respectively, allows us to investigate changes in the spectral continuum as well as the centroids, intrinsic fluxes, equivalent widths, and FWHMs of the spectral lines on a 67 s time-scale, taking into account observing overheads. Fig. 3 displays the evolution of the simultaneous AAVSO *V* and *I* pre-validated magnitudes compared with that of the synthetic magnitudes derived through the convolution of Johnson and Cousins filters with the sub-spectra. It is clear that despite some small discrepancies, the match in *V* is quite good, which confirms the reality of the spectral variability and points towards the flux calibration of each *V* sub-spectrum to be accurate at about 10 per cent. However, differences are larger in *I*, and while the evolutions of both the AAVSO pre-validated and FORS2 synthetic magnitudes are similar, flux discrepancies are wider. We did a similar comparison with the simultaneous *I* magnitudes presented in Kimura et al. (2016) and find the same discrepancies. Large losses are likely mostly due to sky transparency variations, in particular thin clouds passing. However, it is not clear why some of our synthetic magnitudes are significantly smaller, i.e. we find large flux excesses. No problem was reported during the observations, and we are not aware of any extra light entering the slit and/or the detector. The spectro-photometric standard star was moreover observed in similar conditions in both *V* and *I* and its flux calibration is very good. Even if the flux level of the average *I* spectrum is accurate, it is clear that the flux calibration of each individual *I* sub-spectrum was likely compromised, with mild to severe differences with photometric measurements. Although we believe that this does not impact the relevance of the variability pattern, we decided not to investigate the flux variability of the lines present in the *I* sub-spectra. Nonetheless, their equivalent widths and FWHMs being independent on the accuracy of their local continuum, we still trace the changes in these two quantities, although we only consider the *I* sub-spectra for which the difference between the AAVSO and synthetic magnitudes is lower than 0.2 in absolute value.

We thus selected the brightest HI and He I as well as four Fe II features and the way we measured the line parameters differs from that used for the average spectrum. Indeed, to ensure that the choice of continuum had the smallest effect as possible, a given line was fitted, in all the sub-spectra, within the exact same window with a single Gaussian and its base continuum was extrapolated with a first-order polynomial from the exact same wavelengths. Likewise, uncertainties were measured from the real errors as given after the extraction process. The first result is that none of the lines, including the redshifted ones, exhibit detectable centroid variations. Second, there is an obvious correlation between the intrinsic fluxes and local continua (Fig. 4), which clearly hints at a common origin for the continuum and line variability. While this could also be interpreted as an evidence that all the features come from the same component,

Table 2. Optical lines in V404 Cygni FORS2 spectrum. '†' marks the features have a complex continuum making the measurements difficult; '∗' means that the lines are detected but measurements would be unreliable.

Element	λ_c[a]	λ_l[b]	ΔV[c]	$\mathring{W}$[d]	FWHM[e]	F_{line}[f]
			V band			
Fe II	4583.8 ± 1.8	4583.8	–	∗	∗	∗
Fe II+BB	4632.0 ± 3.4	4629–4650	–	∗	∗	∗
He II	4686.4 ± 1.3	4685.9	–	∗	∗	∗
He I	4714.0 ± 2.3	4713.1	–	∗	∗	∗
Hβ	4863.5 ± 0.6	4861.3	123 ± 37	− 264.2 ± 6.0	934 ± 31	277.8 ± 5.4
Fe II	4923.8 ± 0.8	4923.9	–	− 23.7 ± 3.1	631 ± 64	27.5 ± 2.7
Fe II	5018.2 ± 0.6	5018.4	–	− 36.1 ± 5.2	701 ± 61	42.2 ± 4.8
†Si II	5040.0 ± 2.4	5041.0	–	− 10.2 ± 4.1	744 ± 154	12.4 ± 3.3
†Si II	5055.5 ± 2.7	5056.0	–	− 13.6 ± 4.5	940 ± 189	18.2 ± 5.1
Fe II	5169.7 ± 0.7	5169.0	–	− 21.0 ± 2.3	618 ± 62	33.7 ± 4.1
Fe II	5234.4 ± 2.2	5234.6	–	− 4.6 ± 1.6	593 ± 125	7.8 ± 2.3
Fe II	5276.2 ± 1.8	5276.0	–	− 6.6 ± 3.2	563 ± 116	11.3 ± 1.6
Fe II	5316.7 ± 1.0	5316.7	–	− 9.5 ± 1.7	543 ± 112	16.2 ± 2.0
Fe II	5363.2 ± 3.5	5362.8	–	− 1.5 ± 0.5	504 ± 94	3.1 ± 1.7
Fe II	5533.6 ± 4.3	5532.1	–	∗	∗	∗
N II	5678.2 ± 5.1	5679.6	–	∗	∗	∗
He I	5878.1 ± 0.6	5875.6	115 ± 31	− 80.3 ± 4.1	982 ± 59	259.9 ± 10.6
Fe II	6150.2 ± 7.7	6148.0	–	∗	∗	∗
Fe II	6245.4 ± 5.5	6247.6	–	∗	∗	∗
Si II	6347.2 ± 1.7	6347.1	–	− 5.8 ± 1.9	668 ± 135	24.0 ± 5.6
Si II	6370.6 ± 2.1	6371.4	–	− 3.8 ± 1.5	580 ± 241	15.5 ± 4.4
Fe II	6382.9 ± 4.2	6383.4	–	∗	∗	∗
Fe II	6457.4 ± 3.1	6456.4	–	∗	∗	∗
Hα	6564.6 ± 0.2	6562.7	76 ± 10	− 1129.0 ± 4.0	1056 ± 13	5315.1 ± 24.1
He I	6680.9 ± 0.5	6678.2	108 ± 22	− 39.0 ± 3.4	959 ± 31	189.1 ± 6.4
He I	7067.5 ± 0.5	7065.2	85 ± 21	− 40.7 ± 1.5	920 ± 41	247.0 ± 7.4
He I	7283.4 ± 1.0	7281.3	74 ± 41	− 8.2 ± 1.1	809 ± 111	56.9 ± 6.2
			I band			
He I	7068.0 ± 0.3	7065.2	106 ± 13	− 41.8 ± 1.2	906 ± 26	256.8 ± 8.0
He I	7283.7 ± 0.9	7281.3	86 ± 37	− 8.7 ± 0.8	8033 ± 88	60.7 ± 5.6
†O I	7776.6 ± 0.6	7773.4	110 ± 23	− 10.6 ± 1.0	546 ± 48	106.1 ± 6.2
O III	7875.8 ± 6.1	7873.5	–	∗	∗	∗
O II	7897.2 ± 8.1	7894.6	–	∗	∗	∗
?	8223.2 ± 3.8	–	–	∗	∗	∗
†O I	8446.2 ± 1.7	8446.4	–	− 32.8 ± 3.1	740 ± 59	356.0 ± 18.8
†Pa (17-3)	8468.7 ± 2.8	8467.3	–	− 3.5 ± 1.1	462 ± 60	61.0 ± 7.1
Pa (16-3)	8501.1 ± 0.9	8502.5	–	− 24.8 ± 2.5	465 ± 25	218.1 ± 10.8
Pa (15-3)	8544.6 ± 0.8	8545.4	–	− 45.2 ± 4.4	574 ± 32	338.7 ± 12.8
Pa (14-3)	8598.8 ± 0.5	8598.4	–	− 20.7 ± 2.2	585 ± 30	184.4 ± 7.4
Pa (13-3)	8665.6 ± 0.6	8665.0	–	− 48.5 ± 4.0	621 ± 34	463.9 ± 8.9
Pa (12-3)	8751.2 ± 0.5	8750.5	–	− 30.1 ± 2.1	632 ± 35	291.1 ± 9.7
Pa (11-3)	8863.5 ± 0.5	8862.8	–	− 44.6 ± 3.1	676 ± 24	384.3 ± 8.6
Pa (10-3)	9015.9 ± 0.5	9014.9	20 ± 17	− 60.2 ± 3.0	702 ± 30	464.9 ± 22.3
†Pa (9-3)	9230.4 ± 0.8	9229.0	33 ± 26	− 85.8 ± 4.6	927 ± 101	860.6 ± 20.0

Notes. [a]Measured wavelength in Å.
[b]Air laboratory wavelength in Å.
[c]Radial velocity shift in km s^{-1}, corrected for a 13 km s^{-1} heliocentric–barycentric velocity.
[d]Equivalent widths in Å.
[e]Full width at half-maximum in km s^{-1}, quadratically corrected for instrumental broadening.
[f]Intrinsic line flux in units of 10^{-15} erg cm^{-2} s^{-1}.

the evolution of their respective equivalent widths hints at two different behaviours (Fig. 5). Indeed, those of Hα, Hβ, He I λ5876, as well as Fe II λ5169 and λ5317, are unambiguously anticorrelated with their underlying continua, whereas the others show little changes. Likewise, the FWHMs of the first three lines plus those of He I λ6678 and He I λ7065 (in both *V* and *I*) show a similar anticorrelation (Fig. 6), whereas the four Fe II lines have constant FWHMs.

3.3 The X-ray emission

As shown in Table 1, only the last *INTEGRAL* pointing is strictly simultaneous with the FORS2 observations. However, V404 Cygni is barely detected by *INTEGRAL* at this epoch and we can only make use of a 3.6–16 keV JEM-X spectrum. While this is enough to perform a phenomenological spectral fit, it cannot allow us to get a better view of the X-ray properties of the source. This is the reason why we also use the remaining X-ray spectra, which were

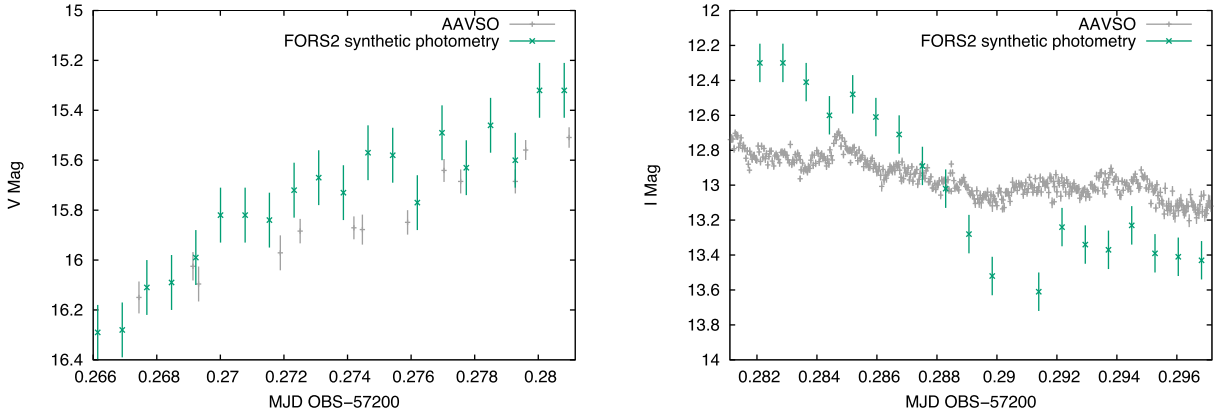

Figure 3. Variations at 67 s time-scale of the *V* (left) and *I* (right) synthetic magnitudes derived from the convolution of V404 Cygni sub-spectra with Johnson and Cousins photometric filters (green). We compare them to the simultaneous pre-validated AAVSO *V* and *I* magnitudes (grey).

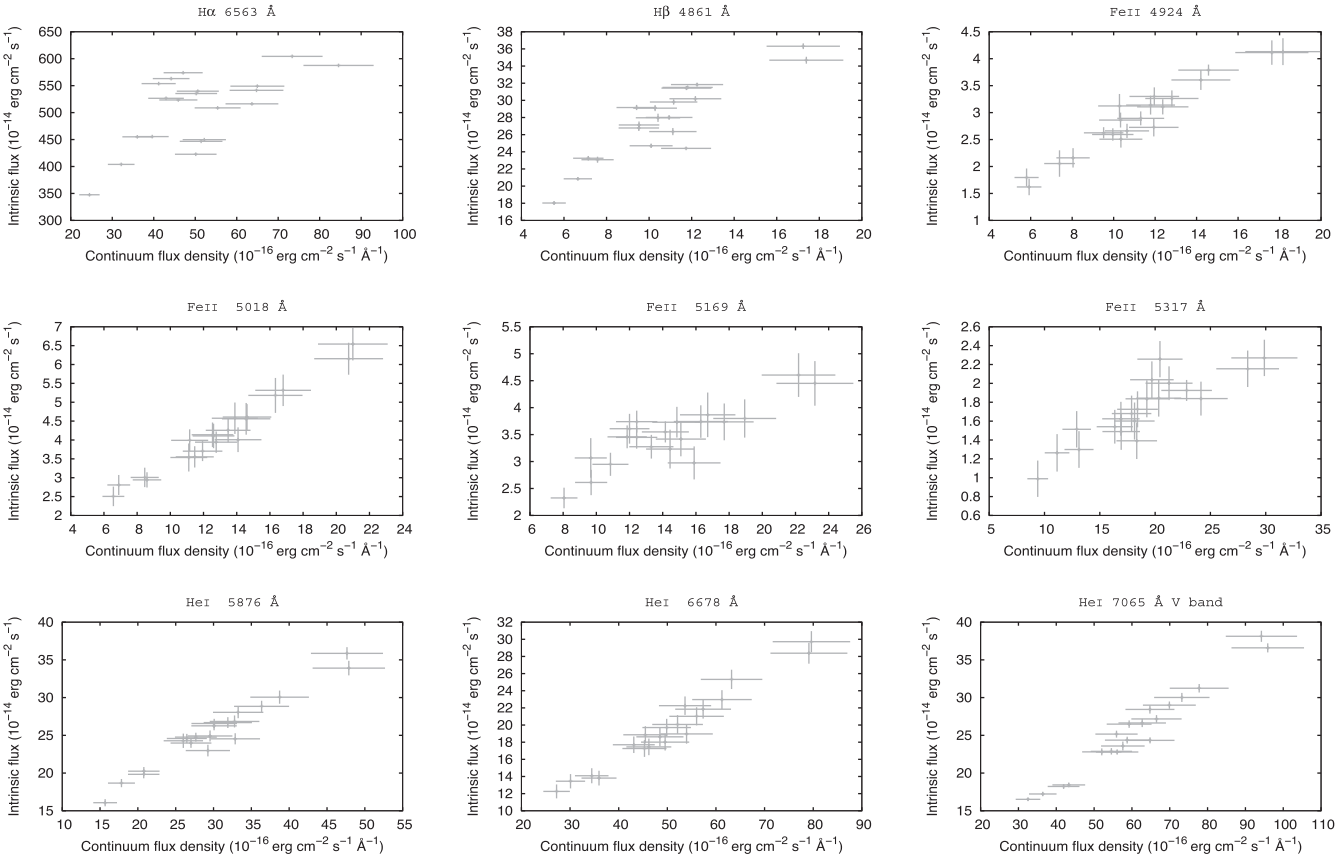

Figure 4. Variations of the intrinsic flux of the emission lines in our sample in function of their underlying continuum.

obtained 0.5 and 2.2 h before. Concerning the non-simultaneity of the X-ray spectra, we stress that we are not interested in performing a very detailed spectral analysis and that our aim here is only to obtain a rough estimate of the nature of the high-energy emission from V404 Cygni.

We first combined the *Swift*/XRT (#00031403061) and *INTEGRAL*/JEM-X+ISGRI (#155700300010) data sets to build a 0.5–150 keV spectrum (hereafter Spec1) and fit it, using XSPEC v. 12.9.0, with a model consisting of a viscous disc (EZDISKBB; Zimmerman et al. 2005) and a spherical Comptonization component (COMPTT; Titarchuk 1994). Both were modified by the ISM extinction, modelled with TBABS for the abundances and cross-sections given in Wilms, Allen & McCray (2000) and Verner et al. (1996), respectively, and multiplicative constants were introduced to take calibration discrepancies into account. We restricted the XRT spectrum to the 0.5–3.2 keV energy range, as including data points up to 5 keV resulted in an abnormally low XRT multiplicative constant. During the fitting process, the seed photon temperature kT_0 of COMPTT was moreover tied to the maximum accretion disc temperature $kT_{\rm max}$. The best-fitting parameters are listed in the first column of Table 3 and the best-fitting model is displayed in the left-hand panel of Fig. 7. The fit is satisfactory, with a reduced χ^2 of 1.02, and points towards a relatively cold accretion disc ($kT_{\rm max} = 0.28 \pm 0.03$ keV) dominating the soft X-rays below 3 keV whereas a warm and thick

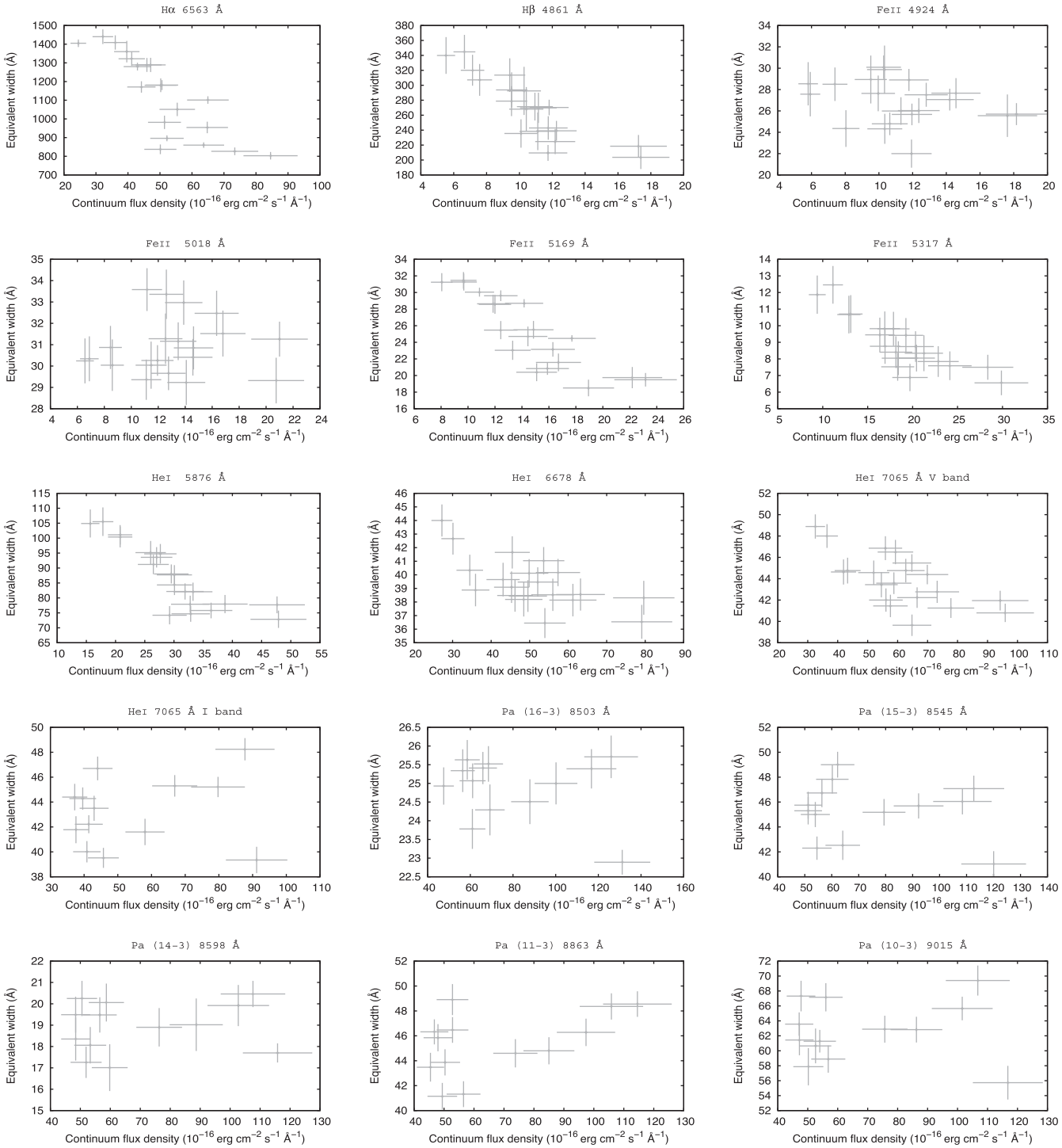

Figure 5. Variations of the equivalent width of the emission lines in our sample in function of their underlying continuum.

Compton component ($kT_e = 39^{+23}_{-7}$ keV and $\tau = 3.46^{+0.66}_{-1.19}$) is responsible for the bulk of the emission beyond 4 keV. The inferred inner radius R_{in} for $f \sim 1.7$ (Shimura & Takahara 1995), $i \sim 67°$, and $M_{BH} \sim 9$ M$_\odot$ as given in Khargharia et al. (2010) ranges between 3 and 6 R_S, i.e. we do not see evidence for significant truncation of the inner accretion disc, although we stress that an $f = 1.7$ value may not be fully appropriate when the hard X-ray continuum dominates the emission (see e.g. Reynolds & Miller 2013). We also note that the derived column density $N_H = 0.85^{+0.10}_{-0.09} \times 10^{22}$ cm^{-2} is consistent with an ISM extinction A_V between 3.4 and 4.3 once converted with the relationship given in Güver & Özel (2009), i.e. a similar value than that derived via optical spectroscopy.

We used the same model to fit the second *INTEGRAL*/JEM-X+ISGRI 3.6–150 keV spectrum (#155700320010, hereafter Spec2) but the lack of soft X-ray data prevented us from constraining the accretion disc parameters. We therefore kept COMPTT only and fixed kT_0 to the value derived for Spec1, assuming that the accretion disc had not significantly cooled down or heated up. We

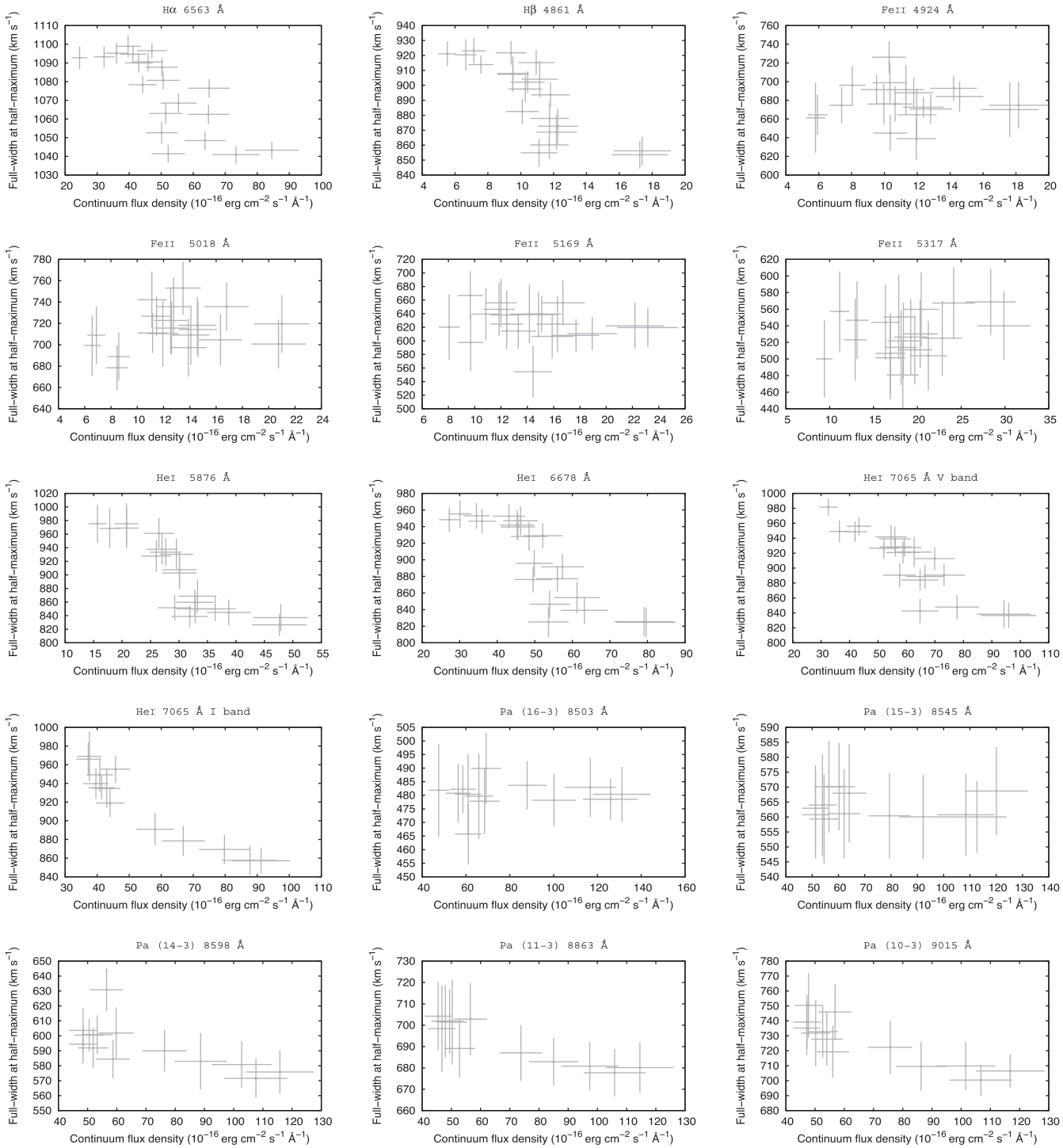

Figure 6. Variations of the FWHM of the emission lines in our sample in function of their underlying continuum.

derive similar parameters (see Table 3, second column, and Fig. 7, middle panel, for the best-fitting parameters and best-fitting model, respectively), and the fit is good, with a reduced χ^2 of 1.12. The only difference with Spec1 is that the 4–150 keV flux is three times higher (3.37×10^{-8} versus 1.13×10^{-8} erg cm^{-2} s^{-1}), hinting at an X-ray variability driven by the Compton component.

Our third 3.6–16 keV JEM-X spectrum, simultaneous with our FORS2 observations (#155700340010, hereafter Spec3), was fitted with an absorbed power law, the column density being fixed to that found for Spec1. The best-fitting parameters are listed in the third column of Table 3 and the best-fitting model is displayed in the right-hand panel of Fig. 7. We find that Spec3 is quite soft, with a photon index $\Gamma = 3.31^{+0.26}_{-0.24}$, and a lot fainter than Spec1 and Spec2, with a 4–15 keV flux of about 0.3×10^{-9} erg cm^{-2} s^{-1} against 2.4×10^{-9} and 5.7×10^{-9} erg cm^{-2} s^{-1}, respectively. For comparison, we also fit the 3.6–16 keV parts of Spec1 and Spec2 with absorbed power laws and find that both spectra are harder than Spec3, with 1.5–2 photon indices. This softening is

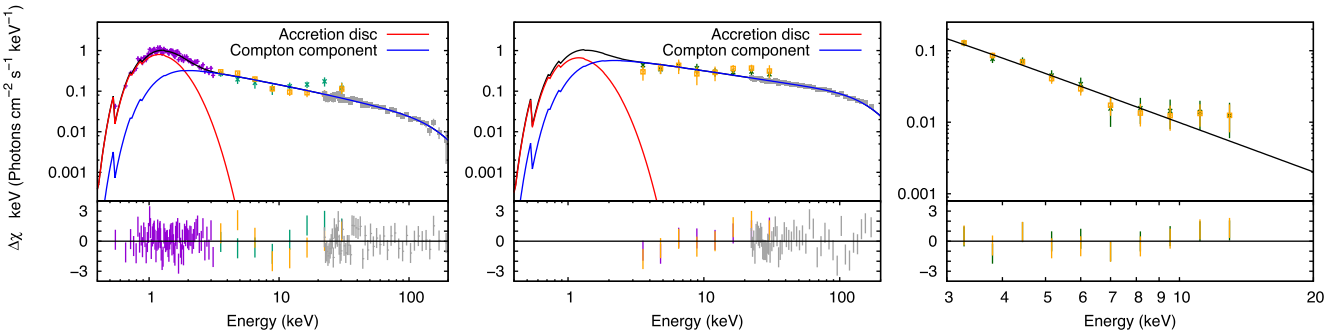

Figure 7. Best fits to the V404 Cygni X-ray spectra combining *Swift*/XRT (magenta) with *INTEGRAL*/JEM-X-1 (green) and JEM-X-2 (orange), and ISGRI (grey) data. Only the third broad-band X-ray spectrum (right) is simultaneous to the FORS2 observations, the two others having been obtained about 2.2 (left) and 0.5 h (middle) before.

Table 3. Best-fitting parameters to the V404 Cygni *Swift*/XRT and *INTEGRAL*/JEM-X+ISGRI combined spectra with TBABS×(EZDISKBB+COMPTT). Spec3 is simultaneous to the FORS2 observations, whereas Spec1 and Spec2 were obtained 2.2 and 0.5 h before, respectively. The error bars are given at the 90 per cent confidence level.

	Spec1	Spec2	Spec3
$N_{\rm H}{}^{a}$	$0.85^{+0.10}_{-0.09}$	0.85 (fixed)	0.85 (fixed)
$kT^{b}_{\rm max}$	0.28 ± 0.03	–	–
$R^{c}_{\rm in}$	$108.1^{+41.9}_{-28.5}$	–	–
kT^{d}_{0}	tied to $kT_{\rm max}$	0.28 (fixed)	–
$kT^{e}_{\rm e}$	$38.5^{+22.7}_{-6.7}$	$36.4^{+2.6}_{-2.1}$	–
τ^{f}	$3.46^{+0.66}_{-1.19}$	$4.41^{+0.22}_{-0.21}$	–
Γ^{g}	–	–	$3.31^{+0.26}_{-0.24}$
$C^{h}_{\rm JMX2}$	$1.21^{+0.23}_{-0.18}$	$0.80^{+0.21}_{-0.18}$	$1.11^{+0.15}_{-0.13}$
$C^{i}_{\rm ISGRI}$	$1.18^{+0.22}_{-0.18}$	$0.99^{+0.16}_{-0.12}$	–
$C^{j}_{\rm XRT}$	$1.01^{+0.22}_{-0.18}$	–	–
F^{k}_{4-15}	0.24	0.57	0.03
F^{l}_{4-150}	1.13	3.37	–
$\chi^2_{\rm r}$ (d.o.f)	1.02 (136)	1.12 (61)	0.76 (17)

Notes. [a]Column density in units of 10^{22} cm^{-2}.
[b]Accretion disc maximum temperature (keV).
[c]Inner radius in units of $f^2 D_{\rm BH}/\sqrt{\cos i}$ km, with i the inclination, $D_{\rm BH}$ the distance in unit of 10 kpc, and f is the colour-to-effective temperature ratio.
[d]Input soft photon temperature (keV).
[e]Electron temperature (keV).
[f]Electron optical depth.
[g]Power-law photon index.
[h]JEM-X-2 multiplicative constant.
[i]ISGRI multiplicative constant.
[j]XRT multiplicative constant.
[k]4–15 keV flux in units of 10^{-8} erg cm^{-2} s^{-1}.
[l]4–150 keV flux in units of 10^{-8} erg cm^{-2} s^{-1}.

likely the reason why V404 Cygni is not detected by IBIS, and assuming that Spec3 also stems from Comptonization, a possible explanation for such a phenomenon is a change in the physical properties of the Compton component. In particular, a steepening of the power law may, for instance, result from a drastic cooling at constant optical thickness or alternatively a drop in opacity at constant temperature. This behaviour may indicate that the source has entered a hard-to-soft transition following a substantial flux decrease between Spec2 and Spec3. These types of transitions have been observed in some persistent microquasars which are predominantly found in the hard state, such as GRS 1758−258 (see e.g. Smith et al. 2001).

4 DISCUSSION

The wealth of HI, He I, and higher ionization lines in V404 Cygni optical spectrum, the strength of the Balmer emission signatures, and the variability pattern at short time-scale are exceptional and confirm the peculiarity of the V404 Cygni outburst with respect to more classical BH XRBs. In the following sections, we investigate the origin of the spectroscopic content and draw a possible scenario to explain this behaviour.

4.1 Where do the emission lines come from?

In outbursting microquasars, optical emission lines are thought to stem from the irradiated chromosphere of the outer accretion disc. In this case and assuming that they are principally rotationally broadened, we have the following relationship between the Keplerian velocity $V_{\rm out}$ at the outer radius $R_{\rm out}$ and their FWHMs (see e.g. Casares 2016):

$$V_{\rm out} \sin i = \sqrt{\frac{GM_{\rm BH}}{R_{\rm out}}} \sin i \leq \frac{\rm FWHM}{2} \ {\rm km\,s^{-1}}, \quad (1)$$

where i is the system's inclination. Although V404 Cygni 's outer radius is unknown, its derived orbital parameters are accurate enough to estimate the typical Keplerian velocities $V_{\rm L}$ and $V_{\rm C}$ at the Roche lobe and circularization radii $R_{\rm L}$ and $R_{\rm C}$, respectively, the former being larger and the latter smaller than $R_{\rm out}$. Using the expressions given in Eggleton (1983) and Frank, King & Raine (2002) as well as the Kepler's third law, we derive:

$$V_{\rm L} \sin i = 4.07\,10^5 \left(\frac{2\pi G f}{P}\right)^{\frac{1}{3}} \sqrt{(1+q)(0.7+q^{\frac{2}{3}}\ln(1+q^{-\frac{1}{3}})} \quad (2)$$

and

$$V_{\rm C} \sin i = 2.85\,10^5 \left(\frac{2\pi G f}{P}\right)^{\frac{1}{3}} (0.5 - 0.227 \log q)^{-2} \quad (3)$$

in km s^{-1}. Here q is the secondary-to-primary mass ratio, P is the orbital period in days, and f is the orbital mass function of the BH in $M_\odot$. For V404 Cygni parameters as given in Casares & Charles (1994) and using equation (1), we can thus conservatively expect typical FWHMs between 400 and 700 km s^{-1} for optical emission lines originating anywhere between the Roche lobe and

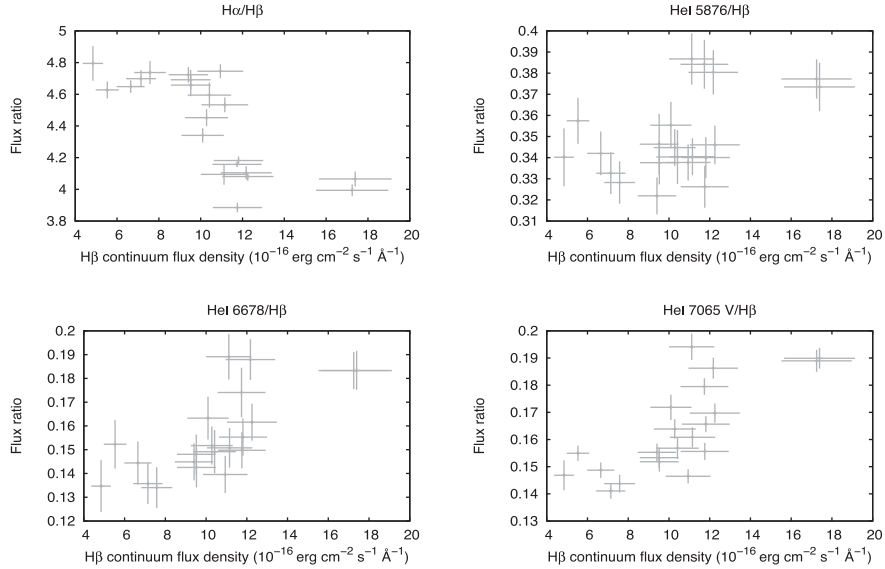

Figure 8. Hα (top left), He I λ5876 (top right), He I λ6678 (bottom left), and He I λ7065 (bottom right) over Hβ flux ratios variations in function of Hβ underlying continuum.

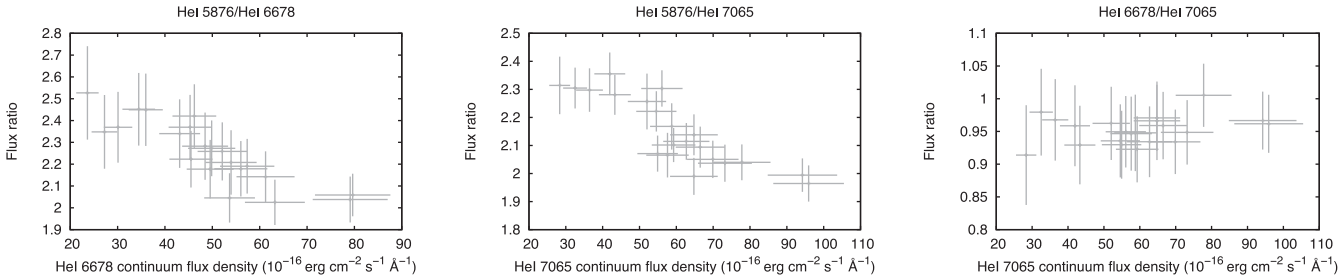

Figure 9. He I λ5876/He I λ6678 (left), He I λ5876/He I λ7065 (middle), and He I λ6678/He I λ7065 (right) flux ratios variations in function of the denominator underlying continuum.

circularization radii (not necessarily the disc), and this is the case for most of the detected features listed in Table 2.

However, Hα, Hβ, He I λ5876, He Iλ6678, and He I λ7065 all are broader, with FWHMs$\geq$900 km s^{-1}, i.e. three to four times closer to the BH if we associate this broadening to a Keplerian rotation. Taking into account that these five HI and He I lines also are the only ones exhibiting significant radial velocity redshifts and anti-correlations between their local continua and both their equivalent widths and FWHMs, we can speculate that they originate from a different emitting region than the outer system. For Hα and Hβ this statement is further strengthened by the average Balmer decrement Hα/Hβ= 4.61 $\pm$ 0.62, measured from the line fluxes corrected for the ISM extinction $A_{\rm V}$ = 3.82 $\pm$ 0.36 as derived in Section 3.1. This value is larger than and inconsistent with the $\approx$3.2 value found just before the outburst initial rise (Bernardini et al. 2016) and the canonical 2.86 for case B recombination of an ionized 10 000 K nebula (Baker & Menzel 1938). It is also very different from unity, which is expected from optically thick irradiated accretion discs found in cataclysmic variables (Williams 1980; Williams & Shipman 1988; Tomsick et al. 2016) and some outbursting microquasars (see e.g. Rahoui, Coriat & Lee 2014). As shown in Drake & Ulrich (1980), a possible explanation for such a large Balmer decrement is the combined effects of high optical depths in the Balmer lines and the relative importance of collisional excitation compared to radiative or recombination processes. This could also explain the anticorrelation between their equivalent widths and local optical continua. Indeed, if the lines are optically thick, any increase in the ionizing radiation enhances their optical depths further, as shown in Ferland & Netzer (1979), and the higher the ionizing field, the flatter their flux evolution. Assuming an optically thin continuum emitting region, which is reasonable considering the broad Hα wings, this phenomenon effectively results in the aforementioned anticorrelation. Incidentally, if optical depth effects really are important, we expect the Hα/Hβ decrement to be anticorrelated to the Hβ local continuum, as Hα optical depth increases at a faster pace, and this is exactly the case (see top-left panel of Fig. 8). In contrast, the variations of the three He I/Hβ decrements in function of Hβ continuum rather show a clear upwards evolution (see the remaining three panels of Fig. 8), which strengthens the hypothesis of a rapid optical depth increase in Hβ. Likewise, He I λ5876/He I λ6678 and He I λ5876/He I λ7065 decrements point towards a similar enhancement for He I λ5876 optical depth, as they evolve upwards too (see Fig. 9). Nonetheless, He I λ6678/He I λ7065 decrement is constant, hinting at the lack of significant optical depth variations, which may explain why the two lines do not exhibit the same unambiguous equivalent width/local continuum anticorrelation.

4.2 A classical nova-like nebula in V404 Cygni?

The same decrement analyses for all the narrow HI and He I lines (FWHM $\sim$400–600 km s^{-1}), which we argue likely stem from the outer regions, do not show any peculiarity and remain constant.

Based on their equivalent widths, large radial velocity redshifts and/or the evolution of their decrements, it is therefore tempting to associate Hα, Hβ, He I λ5876, λ6678, and λ7065 to an expanding broad-line region (BLR) in which collisional processes may be important, lines are optically thick, and the continuum optically thin. But what could this BLR be and how does this relate to the FWHM/local optical continuum anticorrelation? A first explanation is that these FWHM variations trace the irradiation-induced expansion or contraction of the BLR, i.e. a decrease or an increase of its Keplerian velocity, similarly to what we would expect from the inflated base of a Compton-heated ADW (Begelman, McKee & Shields 1983). In this case, the maximum FWHM changes for the lines in *V*, i.e. when the optical continuum is increasing, imply an expansion of the emitting zones of about 20 and 40 per cent, respectively. In contrast, the He I λ7065 FWHM increase in *I*, i.e. when the optical continuum is decreasing, gives a contraction of about 40 per cent. We note that King et al. (2015) reported the X-ray detection of blueshifted emission lines and that P-Cygni profiles were observed in the optical domain (Muñoz-Darias et al. 2016), which favours the ADW base hypothesis. It is however not clear to which extent we really could follow Keplerian velocity variations at such a short time-scale. Moreover, without any better knowledge of the simultaneous X-ray properties of the source, it is difficult to say whether a 20–40 per cent radius increase in less than half an hour is realistic. Another possibility is that FWHM variations are thermally driven, i.e. the narrowing is due to cooling and the broadening to heating. Such an explanation may seem counter-intuitive as cooling and heating would be accompanied by an optical continuum increase and decrease, respectively, but this apparent paradox can be solved if we consider that the emission lines and the continuum arise from the same component and that the emission stems from optically thin bremsstrahlung or synchrotron.

A third alternative, which would reconcile the two aforementioned scenarios, is the presence of a quasi-spherical optically thin nebula surrounding V404 Cygni, which was also proposed by Muñoz-Darias et al. (2016). Indeed, the optical spectrum strongly resembles that of Fe II-type classical novae in their post-outburst nebular phase (see Shore 2008, for a review). This phase is thought to occur once fast and optically thick ADWs stop being fuelled and massively ejected following a significant drop in mass-accretion rate and X-ray ionizing emission. Their outer shell, previously formed, then starts growing and cooling down, becoming optically thin in the process and effectively turning into a nebula, while remnant inner optically thick ADWs keep expanding for some time. Moreover, large Balmer decrement and equivalent width/continuum anticorrelations are also seen and explained in a similar way as we do for V404 Cygni, and a narrowing with time of the broad emission lines is also observed. This narrowing is mainly thought to stem from shocks occurring between the nebulae and much slower stellar winds. In the V404 Cygni case, we can expect slow winds from its cool sub-giant companion star, and the presence of many narrow Fe II emission lines, which behave differently from both the broad features and the other HI and He I signatures, hints at the existence of a stellar winds/nebula front, as suggested in Williams (2012) for classical novae. However, it is important to remember that our data suggest not only a narrowing when the continuum is increasing, but also a broadening when it is decreasing. The spectroscopic content is also divided between narrow stationary features and broad redshifted ones. Thus, another explanation that could account for both could be that the broad lines actually originate from deeper in the nebula, in a region, which could be the remnant ADW, moving faster than the outer optically thin shell and eventually colliding with it. The collision leads to the temporary narrowing of the thick emission lines, which re-broaden once the interaction is over because we see deeper in the nebula again.

4.3 The origin of optical continuum

In the soft state, the optical continuum of outbursting low-mass XRBs is usually dominated by the viscous or reprocessed emission of the accretion disc, to which synchrotron radiation from the compact jets is added in the hard state. The companion star contribution may also be detectable but only when the source is close to quiescence. In the ν versusF_ν plan, this leads to a blue continuum from the disc, with a spectral index between roughly 0.3 and 2, and a potential red excess when jets are present (see e.g. Rahoui et al. 2012, 2015, in the case of GX 339−4 and Swift J1753.5-0127).

Fig. 10 displays the extinction-corrected average continuum of V404 Cygni during our observations, corrected for the companion star emission, and it is clear that it does not correspond to the previous description. Indeed, it is characterized by a red increase and a blue exponential decay with rough spectral indices of +2 and −1.5, respectively, the turnover being located around 3.5×10^{14} Hz. We therefore performed a phenomenological fit of the V404 Cygni optical continuum with a function consisting of a power law of spectral index α up to frequency turnover ν_c and an exponential decay of temperature *T* beyond. To better constrain the fit, we also use the *Swift*/UVOT *U* and REM *J*, *H*, and K_s fluxes, all corrected for the companion star emission. The best fit is displayed in Fig. 10, to which we superimposed the contemporaneous radio and sub-millimetre fluxes obtained with RATAN-600 and NOEMA as well as the simultaneous JEM-X spectrum to build the radio to X-ray SED. We infer $\alpha \approx 1.86$, consistent with a Raleigh–Jeans tail, $\nu_c \approx 3.64 \times 10^{14}$ Hz, and $T \approx 14\,000$ K, which is cool enough for Balmer and He I emission line formation. Moreover, while the fit correctly accounts for the *J*-band flux density, a near-IR excess is present. Based on the radio and sub-millimetre flux levels and decay (−0.62 spectral index), this excess does not appear to stem from optically thin synchrotron from the compact jets, but the variability of the source is such that we believe it cannot be excluded. A dusty component might also account for this mismatch.

Our phenomenological fit confirms the peculiarity of the V404 Cygni optical spectrum with respect to other microquasars. But which physical processes does it describe? A first possibility is self-absorbed optically thin cyclo-synchrotron emission, similarly to that modelled for a magnetized corona above the accretion disc in Di Matteo, Celotti & Fabian (1997). However, for BH XRBs, such a mechanism is expected to peak in the UV domain, between 10^{15} and 10^{16} Hz, and a peak around 3.6×10^{14} Hz would yield very high magnetic field strengths $B \geq 10^7$ G and/or temperatures $T \geq 10^6$ K (Wardziński & Zdziarski 2000). Similarly, optically thin synchrotron from an advection-dominated accretion flow (Narayan & Yi 1995) was successfully used in quiescent sources but it is likely not applicable to an outbursting microquasar at the very beginning of the decay, especially considering that the mass-accretion rate we derive from our X-ray fit is $\dot{M}_{\rm acc} \approx 0.01 \dot{M}_{\rm Edd}$ for Khargharia et al. (2010) parameters and $f = 1.7$. In place of synchrotron-related phenomena, we rather believe that a more realistic physical process is self-absorbed optically thin bremsstrahlung, which gives rise to continuum radiation very similar to observed from V404 Cygni. If true, it is tempting to associate this free–free emission to the geometry of the ADW cooling remnant we claim is present. Indeed, it is noteworthy that a consequence of shocks between slower optically thin and faster optically thick regions is the conversion of kinetic

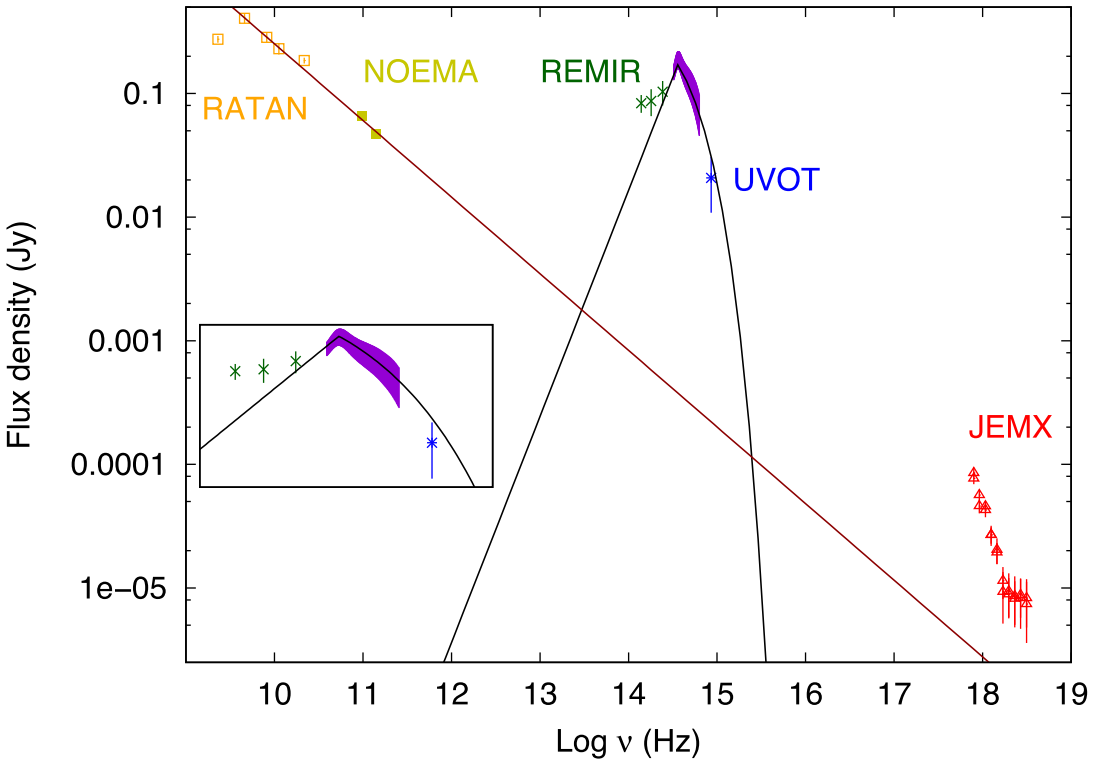

Figure 10. V404 Cygni SED modelled with a self-absorbed optically thin bremsstrahlung in the optical and near-infrared domain. A −0.62 spectral index power law, consistent with optically thin synchrotron, is superimposed on the RATAN-600 AND NOEMA radio and sub-millimetre contemporaneous data. The inset displays a zoom-in centred on the REMIR, FORS2 and UVOT data.

energy losses into a optically thin continuum emission, which would likely be bremsstrahlung. Using the expression of the free–free normalization as given in Rybicki & Lightman (1979), we infer an electron density $n_e \approx 10^{10}$ cm^{-3} from our phenomenological fit, assuming that the nebula extends up to the accretion disc Roche lobe radius, which points towards a low density. Incidentally, the shocks between faster and slower regions could also explain why the narrowing and broadening are anticorrelated to the local continua of the emission lines.

5 SUMMARY AND CONCLUSION

We have presented a comprehensive study of the V404 Cygni optical spectrum at the very beginning of its 2015 outburst decay. The high S/N of each individual spectrum as well as the short exposure time has allowed us to perform a thorough analysis of the continuum and spectral variability pattern and to investigate the origin of the existing correlations. We find that the spectral features may originate in three different regions: (1) a fast-moving optically thick plasma, likely an ADW remnant, within a classical nova-like nebula for the broadest (FWHM∼900–1000 km s^{-1}) and redshifted (ΔV ∼ 70–120 km s^{-1}) emission lines; (2) the slow-moving or stationary optically thin outer shell of the aforementioned nebula for the narrow high ionization emission lines (FWHM∼400–600 km s^{-1}); and (3) the outer accretion disc for the remaining narrow H I and He I features. This geometry assumes the existence of a massive, almost discrete optically thick ADW that was turned off prior to the decay and was detected via X-ray emission lines and optical P-Cygni profiles. We further argue that the optical continuum is unlike any observed in other BH XRBs and likely arises from the aforementioned shocks, perhaps through optically thin bremsstrahlung cooling.

Our results confirm the uniqueness of this V404 Cygni outburst in the microquasar family and point towards the dominant role played by massive ADW ejecta in the source properties. It is not clear if these ejecta can be held responsible for part of the extreme flaring activity the source exhibited during its outburst, or if they are only a consequence of the strong flares irradiating the accretion disc. In either case, the reasons behind this behaviour are unknown, but it is noteworthy that V404 Cygni, like the other extreme microquasar GRS 1915+105, is characterized by a long orbital period and a very large accretion disc, which, according to Kimura et al. (2016), could prevent sustained accretion in the inner regions and induce large disc instabilities. Whether or not this is the case, we note that V404 Cygni behaviour, including the various observed anti-correlations, is seen not only in the classical novae from which we draw a parallel, but also in some active galactic nucleus and Seyfert galaxies (see e.g. Lee et al. 2013) with the well-known Baldwin effect (Baldwin 1977). This may point towards the importance of the universal presence of BLRs in accreting systems spanning whole compact object mass scale.

ACKNOWLEDGEMENTS

We are very thankful to the referee for his/her very insightful comments and suggestions that helped improve this paper a lot. We also thank Mariko Kimura for kindly providing her *I*-band photometry. We acknowledge with thanks the variable star observations from the AAVSO International Database contributed by observers worldwide and used in this research. PC acknowledges support by a Marie Curie FP7-Reintegration-Grants under contract no. 2012-322259. This research has made use of data obtained from the High Energy Astrophysics Science Archive Research Center (HEASARC),

provided by NASA's Goddard Space Flight Center. This research has made use of NASA's Astrophysics Data System, of the SIMBAD, and VizieR data bases operated at CDS, Strasbourg, France.

NOTE ADDED IN PROOF

It came to our attention that the Swift/XRT data we use in the first X-ray fit (Table 3, second column; Figure 7, left panel) were also compromised by the dust-scattering halo (A. Beardmore, private communication). While this does not change anything to the results presented in this study, we warn the reader that the derived accretion disc parameters must therefore be considered as incorrect.

REFERENCES

Appenzeller I. et al., 1998, The Messenger, 94, 1
Baker J. G., Menzel D. H., 1938, ApJ, 88, 52
Baldwin J. A., 1977, ApJ, 214, 679
Barthelmy S. D. et al., 2005, Space Sci. Rev., 120, 143
Barthelmy S. D., D'Ai A., D'Avanzo P., Krimm H. A., Lien A. Y., Marshall F. E., Maselli A., Siegel M. H., 2015, GCN Circ., 17929
Beardmore A. P., Altamirano D., Kuulkers E., Motta S. E., Osborne J. P., Page K. L., Sivakoff G. R., Vaughan S. A., 2015, Astron. Telegram, 7736
Begelman M. C., McKee C. F., Shields G. A., 1983, ApJ, 271, 70
Bernardini F., Russell D. M., Shaw A. W., Lewis F., Charles P. A., Koljonen K. I. I., Lasota J. P., Casares J., 2016, ApJ, 818, L5
Burrows D. N. et al., 2005, Space Sci. Rev., 120, 165
Calzoletti L. et al., 2005, Nuovo Cimento C Geophys. Space Phys. C, 28, 759
Casares J., Charles P. A., 1994, MNRAS, 271, L5
Casares J., Charles P. A., Jones D. H. P., Rutten R. G. M., Callanan P. J., 1991, MNRAS, 250, 712
Casares J., Charles P. A., Naylor T., 1992, Nature, 355, 614
Casares J., Charles P. A., Naylor T., Pavlenko E. P., 1993, MNRAS, 265, 834
Casares J., 2016, ApJ, 822, 99
Di Matteo T., Celotti A., Fabian A. C., 1997, MNRAS, 291, 805
Drake S. A., Ulrich R. K., 1980, ApJS, 42, 351
Eggleton P. P., 1983, ApJ, 268, 368
Fender R. P., Belloni T. M., Gallo E., 2004, MNRAS, 355, 1105
Ferland G., Netzer H., 1979, ApJ, 229, 274
Filippenko A. V., 1982, PASP, 94, 715
Frank J., King A., Raine D. J., 2002, Accretion Power in Astrophysics. Cambridge Univ. Press, Cambridge
Freudling W., Romaniello M., Bramich D. M., Ballester P., Forchi V., García-Dabló C. E., Moehler S., Neeser M. J., 2013, A&A, 559, A96
Gandhi P. et al., 2016, MNRAS, 459, 554
Gehrels N. et al., 2004, ApJ, 611, 1005
Gotthelf E., Halpern J. P., Patterson J., Rich R. M., 1992, AJ, 103, 219
Güver T., Özel F., 2009, MNRAS, 400, 2050
Herbig G. H., 1975, ApJ, 196, 129
Hynes R. I., Bradley C. K., Rupen M., Gallo E., Fender R. P., Casares J., Zurita C., 2009, MNRAS, 399, 2239
Jenke P. A. et al., 2016, ApJ, 826, 37
Jenniskens P., Desert F.-X., 1994, A&AS, 106, 39
Khargharia J., Froning C. S., Robinson E. L., 2010, ApJ, 716, 1105
Kimura M. et al., 2016, Nature, 529, 54
King A. L., Miller J. M., Raymond J., Reynolds M. T., Morningstar W., 2015, ApJ, 813, L37
Lebrun F. et al., 2003, A&A, 411, L141
Lee J. C. et al., 2013, MNRAS, 430, 2650
Lund N. et al., 2003, A&A, 411, L231
Marshall D. J., Robin A. C., Reylé C., Schultheis M., Picaud S., 2006, A&A, 453, 635
Martí J., Luque-Escamilla P. L., García-Hernández M. T., 2016, A&A, 586, A58
Martinez P., Kolb J., Sarazin M., Tokovinin A., 2010, The Messenger, 141, 5
Miller-Jones J. C. A., Jonker P. G., Dhawan V., Brisken W., Rupen M. P., Nelemans G., Gallo E., 2009, ApJ, 706, L230
Mooley K., Clarke F., Fender R., 2015, The Astronomer's Telegram, 7714
Muñoz-Darias T. et al., 2016, Nature, 534, 75
Narayan R., Yi I., 1995, ApJ, 452, 710
Natalucci L., Fiocchi M., Bazzano A., Ubertini P., Roques J.-P., Jourdain E., 2015, ApJ, 813, L21
Radhika D., Nandi A., Agrawal V. K., Mandal S., 2016, MNRAS, 462, 1834
Rahoui F. et al., 2012, MNRAS, 422, 2202
Rahoui F., Coriat M., Lee J. C., 2014, MNRAS, 442, 1610
Rahoui F. et al., 2015, ApJ, 810, 161
Rana V. et al., 2016, ApJ, 821, 103
Reynolds M. T., Miller J. M., 2013, ApJ, 769, 16
Rodriguez J. et al., 2015, A&A, 581, L9
Roming P. W. A. et al., 2005, Space Sci. Rev., 120, 95
Rybicki G. B., Lightman A. P., 1979, Astron. Q., 3, 199
Shahbaz T., Ringwald F. A., Bunn J. C., Naylor T., Charles P. A., Casares J., 1994, MNRAS, 271, L10
Shimura T., Takahara F., 1995, ApJ, 445, 780
Shore S. N., 2008, in Bode M. F., Evans A., eds, Classical Novae, 2nd edn. Cambridge Univ. Press, Cambridge, p. 194
Skrutskie M. F. et al., 2006, AJ, 131, 1163
Smith D. M., Heindl W. A., Markwardt C. B., Swank J. H., 2001, ApJ, 554, L41
Stetson P. B., 1987, PASP, 99, 191
Testa V. et al., 2004, in Lewis H., Raffi G., eds, Proc. SPIE, Vol. 5496, Advanced Software, Control, and Communication Systems for Astronomy. p. 729
Tetarenko A., Sivakoff G. R., Bremer M., Miller-Jones J. C., Mooley K., Fender R., Staley T., Anderson G., 2015a, The Astronomer's Telegram, 7740
Tetarenko A., Sivakoff G. R., Young K., Wouterloot J. G. A., Miller-Jones J. C., 2015b, The Astronomer's Telegram, 7708
Titarchuk L., 1994, ApJ, 434, 570
Tomsick J. A., Krivonos R., Wang Q., Bodaghee A., Chaty S., Rahoui F., Rodriguez J., Fornasini F. M., 2016, ApJ, 816, 38
Trushkin S. A., Nizhelskij N. A., Tsybulev P. G., 2015, The Astronomer's Telegram, 7716
Ubertini P. et al., 2003, A&A, 411, L131
Vasilopoulos G., Petropoulou M., 2016, MNRAS, 455, 4426
Verner D. A., Ferland G. J., Korista K. T., Yakovlev D. G., 1996, ApJ, 465, 487
Wagner R. M., Bertram R., Starrfield S. G., Howell S. B., Kreidl T. J., Bus S. J., Cassatella A., Fried R., 1991, ApJ, 378, 293
Wardziński G., Zdziarski A. A., 2000, MNRAS, 314, 183
Williams G. A., Shipman H. L., 1988, ApJ, 326, 738
Williams R., 2012, AJ, 144, 98
Williams R. E., 1980, ApJ, 235, 939
Wilms J., Allen A., McCray R., 2000, ApJ, 542, 914
Winkler C. et al., 2003, A&A, 411, L1
Zimmerman E. R., Narayan R., McClintock J. E., Miller J. M., 2005, ApJ, 618, 832

This paper has been typeset from a TEX/LATEX file prepared by the author.